

# Stabilization of the VO<sub>2</sub>(M2) Phase and Change in Lattice Parameters at the Phase Transition Temperature of W<sub>x</sub>V<sub>1-x</sub>O<sub>2</sub> Thin Films

Artitsupa Boontan, Eric Kumi Barimah,\* Paul Steenson, and Gin Jose

Cite This: *ACS Appl. Mater. Interfaces* 2023, 15, 51606–51616

Read Online

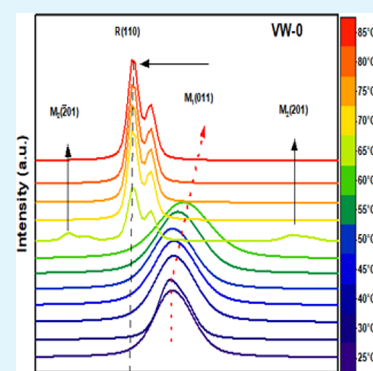
ACCESS |

Metrics &amp; More

Article Recommendations

**ABSTRACT:** Various methods have been used to fabricate vanadium dioxide (VO<sub>2</sub>) thin films exhibiting polymorph phases and an identical chemical formula suited to different applications. Most fabrication techniques require post-annealing to convert the amorphous VO<sub>2</sub> thin film into the VO<sub>2</sub> (M1) phase. In this study, we provide a temperature-dependent XRD analysis that confirms the change in lattice parameters responsible for the metal-to-insulator transition as the structure undergoes a monoclinic to the tetragonal phase transition. In our study, we deposited VO<sub>2</sub> and W-doped VO<sub>2</sub> thin films onto silica substrates using a high repetition rate (10 kHz) fs-PLD deposition without post-annealing. The XRD patterns measured at room temperature revealed stabilization of the monoclinic M2 phase by W<sup>6+</sup> doping VO<sub>2</sub>. We developed an alternative approach to determine the phase transition temperatures using temperature-dependent X-ray diffraction measurements to evaluate the *a* and *b* lattice parameters for the monoclinic and rutile phases. The *a* and *b* lattice parameters versus temperature revealed phase transition temperature reduction from ~66 to 38 °C when the W<sup>6+</sup> concentration increases. This study provides a novel unorthodox technique to characterize and evaluate the structural phase transitions seen on VO<sub>2</sub> thin films.

**KEYWORDS:** fs-PLD, vanadium dioxide, M1 and M2 phases, doping, W, phase transition



## 1. INTRODUCTION

Over the past few decades, numerous polymorph phases of vanadium dioxide (VO<sub>2</sub>) thin films with an identical chemical formula, such as VO<sub>2</sub>(M1), VO<sub>2</sub>(M2), VO<sub>2</sub>(R), VO<sub>2</sub>(A), VO<sub>2</sub>(B), VO<sub>2</sub>(C), VO<sub>2</sub>(D), VO<sub>2</sub>(P), VO<sub>2</sub>(R), and VO<sub>2</sub>(T), have been fabricated, and their properties were studied.<sup>1,2</sup> The formation of various V–O systems can be attributed to different V and O atom sites in the crystalline lattice of coordination polyhedral.<sup>3</sup> These polymorph phases can be transformed into other phases under certain conditions and with different transition temperatures.<sup>1</sup> For instance, VO<sub>2</sub> (D) can undergo a VO<sub>2</sub>(R) phase transformation at a transition temperature of ~320 °C, while VO<sub>2</sub>(A) and VO<sub>2</sub>(B) to VO<sub>2</sub>(R) phase transition temperatures occur at 475 °C.<sup>1</sup> However, the phase transitions of these polymorphs are not reversible by either reducing or rising temperature due to changes in the structural and immense strain or stress transformation. On the other hand, the monoclinic VO<sub>2</sub>(M1) phase has been studied extensively during the last few decades because it undergoes an abrupt metal–insulator transition (MIT) at ~68 °C,<sup>2,3</sup> which is reversible by altering the temperature, the electrical field, incident illumination, and pressure strain properties. Such reversible phase transition temperatures are associated with structural modification from a low-temperature monoclinic M1-phase to a high-temperature rutile R-phase.<sup>3</sup> An intermediate

VO<sub>2</sub>(M2) polymorph phase with a  $\beta$ -angle of 91.88° could be stabilized at room temperature or exist during the MIT from M1 → M2 → R. This can be achieved by doping with a low concentration of various transition elements, such as W, Al, etc., and introducing strain in the film.<sup>4,5</sup>

Meanwhile, VO<sub>2</sub>(M1) has a phase transition temperature slightly higher than room temperature, arguably limiting its practical applications. As a result, several fabrication techniques have been adopted to reduce the VO<sub>2</sub>(M1) phase transition temperature to near room temperature by doping with high-valent transition metals such as Al<sup>3+</sup>, Ta<sup>5+</sup>, Mo<sup>6+</sup>, Nb<sup>5+</sup>, and W<sup>6+</sup>.<sup>5–11</sup> Alternatively, to doping VO<sub>2</sub> with transition metals; the phase transition temperature can be controlled by changing particle sizes, surface morphologies, and crystalline phases during the competitive nucleation growth mechanism.<sup>9</sup> On the other hand, doping with high-valent transition metals of the VO<sub>2</sub> thin films leads to lattice distortion and thus induces local stress

**Received:** August 3, 2023  
**Revised:** October 11, 2023  
**Accepted:** October 12, 2023  
**Published:** October 24, 2023



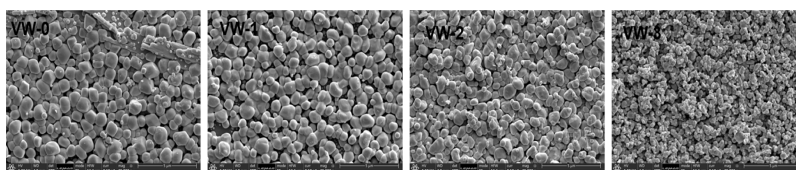


Figure 1. Surface morphology of top-view SEM images of the undoped and W-doped VO<sub>2</sub> thin films.

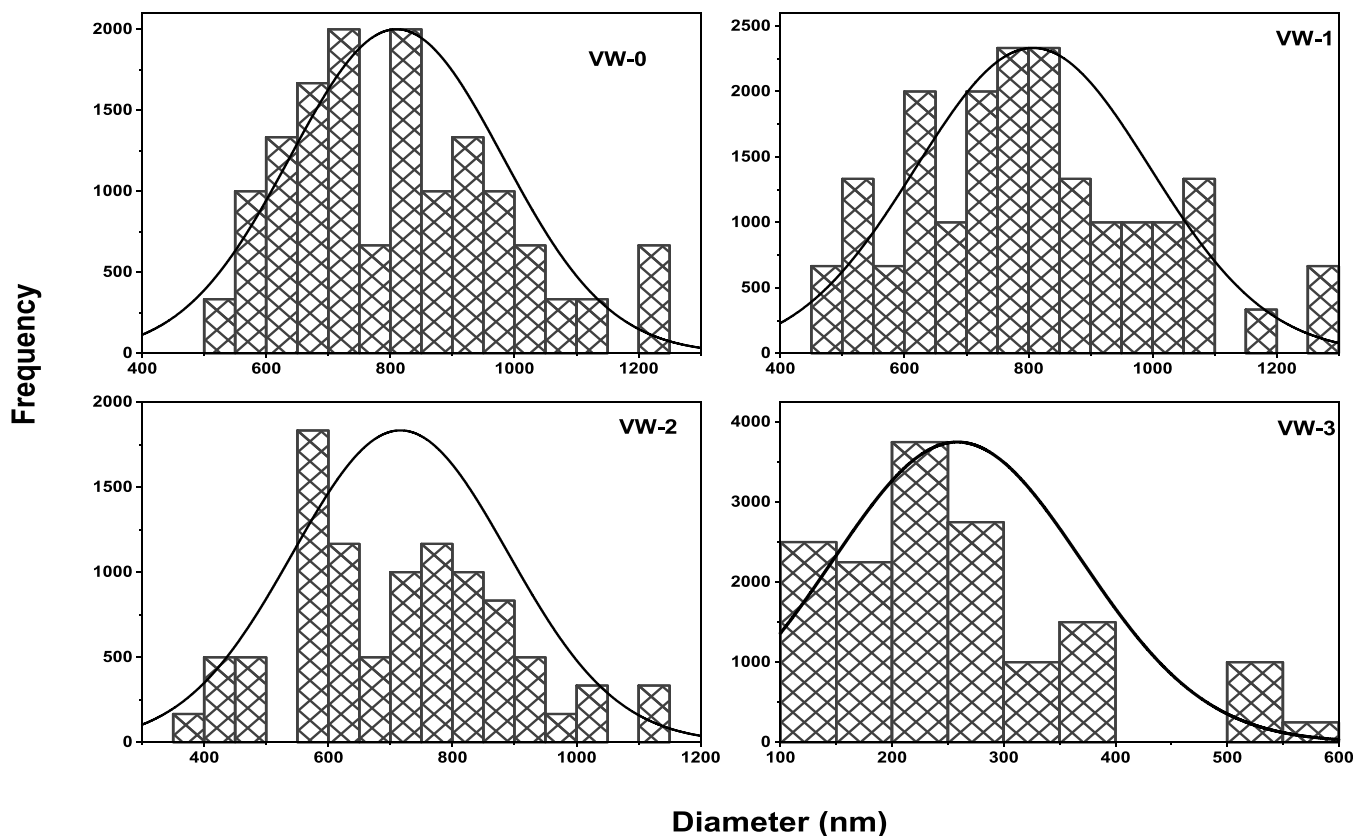


Figure 2. Histogram showing the particle size distribution of undoped and W-doped VO<sub>2</sub> thin films for samples VW-0, VW-1, VW-2, and VW-3.

and strain, which have been shown to reduce the phase transition temperature.<sup>10–14</sup> Thus, lowering the phase transition temperature of VO<sub>2</sub> thin films is attractive for numerous applications such as IR uncooled bolometers, thermochromic coatings, optical switching devices, ultrafast switching, smart radiator devices for spacecraft, and Mott transition field effect transistor.<sup>3,6,7</sup> Recently, there have been a few studies on pure VO<sub>2</sub>(B) and VO<sub>2</sub>(M1) materials, focusing on structural unit cell *a*, *b*, and *c* lattice parameters to determine the MIT behavior and transition temperature.<sup>15,16</sup>

Different techniques have been implemented to fabricate VO<sub>2</sub> and transition metal-doped VO<sub>2</sub> thin films, aiming to lower their transition temperatures, which include sputtering, hydrothermal, nanosecond laser (ns) PLD,<sup>9–11</sup> RF-magnetron sputtering, and femtosecond (fs) PLD.<sup>3,17</sup> Chen et al.<sup>11</sup> synthesized Al<sup>3+</sup>-doped VO<sub>2</sub> thin film onto silicon and soda-lime substrates using Al-doped V<sub>2</sub>O<sub>5</sub> target and ns-PLD with a KrF excimer laser at a wavelength of 248 nm. A transition temperature of 40 °C was reported for VO<sub>2</sub> doped with an Al<sup>3+</sup> thin film compared to 67 °C for the pure VO<sub>2</sub> thin films. Similarly, VO<sub>2</sub> and W<sub>x</sub>V<sub>1-x</sub>O<sub>2</sub> thin films deposited were fabricated with a reactive pulsed laser deposition and a XeCl excimer ns-laser at a wavelength of 308 nm by Soltani et al.<sup>12</sup>

They observed a transition temperature of about 36 and 68 °C for W-doped VO<sub>2</sub> and VO<sub>2</sub> thin films, respectively.

In this study, we fabricated the VO<sub>2</sub> and W<sub>x</sub>V<sub>1-x</sub>O<sub>2</sub> thin films onto a silica substrate without post-annealing using femtosecond pulsed laser deposition at a repetition rate of 10 kHz. We systematically investigated the crystal structure of the VO<sub>2</sub> and W<sub>x</sub>V<sub>1-x</sub>O<sub>2</sub> films by using TEM and XRD patterns. In addition, the FullProf Software was utilized to analyze the temperature-dependent XRD pattern data to evaluate the *a* and *b* lattice parameters and to predict the phase transition temperatures of these samples.

## 2. EXPERIMENTAL METHODS

**2.1. Sample Preparation and Fabrication.** Vanadium pentoxide (V<sub>2</sub>O<sub>5</sub>) and W<sup>6+</sup>-doped vanadium pentoxide (V<sub>2</sub>O<sub>5</sub>) targets with the molar composition of (100 - *x*) V<sub>2</sub>O<sub>5</sub>-*x*WO<sub>3</sub> (*x* = 0, 0.5, 1.0, and 1.5 mol %, namely, VW0, VW1, VW2, and VW3) were prepared. High-purity V<sub>2</sub>O<sub>5</sub> (≥99.99%) and WO<sub>3</sub> (99.99%) materials were purchased from Alfa Aesar. About 25 g batch of pure V<sub>2</sub>O<sub>5</sub> powder and the appropriate amount of WO<sub>3</sub> and V<sub>2</sub>O<sub>5</sub> powders were weighed to prepare W-doped V<sub>2</sub>O<sub>5</sub> powder material. The WO<sub>3</sub> and V<sub>2</sub>O<sub>5</sub> powders were thoroughly mixed using a mortar and a pestle until a homogeneous mixture was obtained. Each powder sample was pressed into a pallet (PLD target) with dimensions of 30 mm × 40 mm × 2 mm using a Spec press with a 1 t load for 5 min. An ultrasonic bath was used to clean the

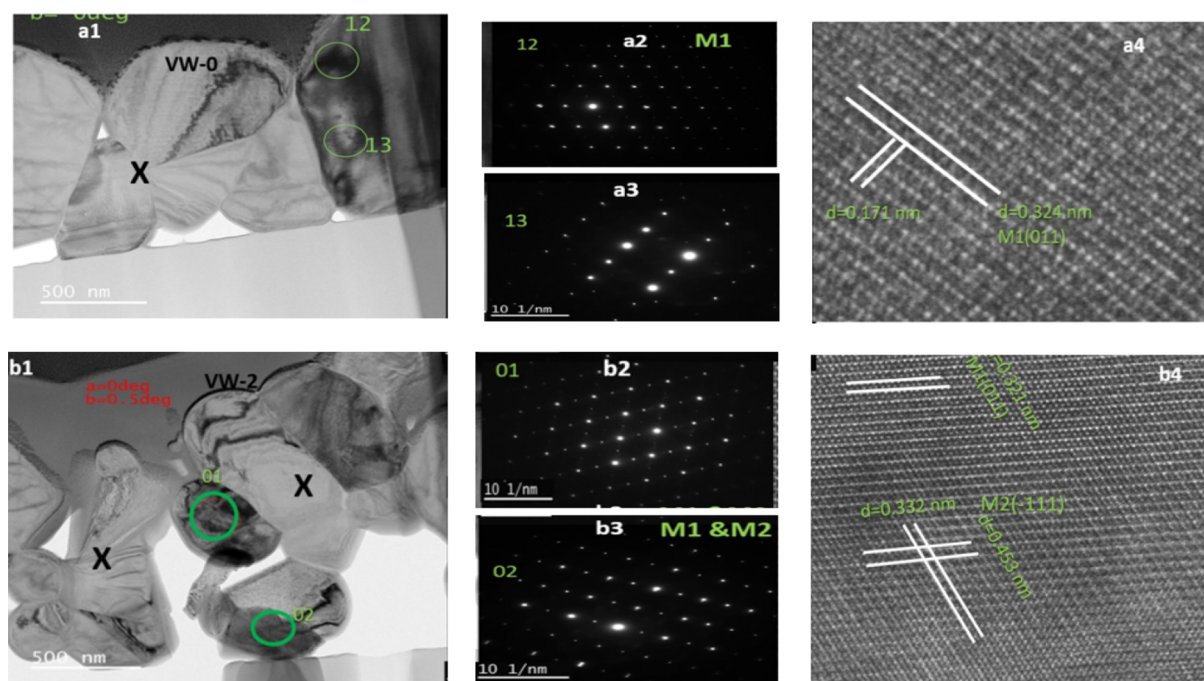


**Figure 3.** (a1, b1) TEM cross-sectional image of samples VW-0 and VW-2; (a2, a3, b2, b3) corresponding SAED patterns of two different areas; (a4, b4) HRTEM images for resolving the VO<sub>2</sub> crystal lattices.

20 mm, 30 mm × 1 mm silica substrates at 50 °C followed by an acetone and isopropyl alcohol rinse and dried with a high-purity nitrogen gas-gun. The substrate and the target were mounted into respective holders within the PLD chamber. The PLD chamber was then evacuated to a base pressure of 10<sup>-7</sup> Torr before backfilling to a working pressure of 70 mTorr using high-purity process oxygen (99.99%). The separation distance from the substrate to the target was kept at 60 mm, and the substrate temperature was maintained at 700 °C. Pure V<sub>2</sub>O<sub>5</sub> and W-doped V<sub>2</sub>O<sub>5</sub> targets were ablated to deposit thin films with a KMLabs Wyvern 1000–10 solid-state Ti:sapphire laser/amplifier and a laser fluence of 0.27 J/cm<sup>2</sup> at a 75 kHz repetition rate. The total deposition time was in the region of 2 h.

**2.2. Characterization.** The surface topography was examined and recorded using a Carl Zeiss EVO MA15 scanning electron microscopy (SEM). Following the SEM imaging, ImageJ software was utilized to determine isolated particle distribution deposited on the substrate. A focused ion beam (FIB) (FEI Helios G4 CX DualBeam) machine was employed to prepare an in situ TEM cross section of each thin film. The FEI Tecnai TF20 transmission electron microscope fitted with a HAADF detector was utilized to acquire cross-sectional images, together with high reflectance TEM images and selected area electron diffraction (SAED) patterns. The room temperature X-ray diffraction patterns of the as-prepared samples were recorded using a P'Analytical X'Pert diffractometer (Cu Kα<sub>1</sub> radiation = 1.54056 Å) at 45 kV and 40 mA. The XRD patterns were measured from 10 to 60° with a step size of 0.02 for angle 2θ. Subsequently, the temperature-dependent studies of XRD patterns were collected using a Malvern P'Analytical Empyrean Diffractometer (CuKα<sub>1</sub> radiation = 1.54056 Å) system equipped with an Anton Parr HTK1200 heating stage unit. The temperature dependent XRD data was recorded in the temperature ranging from 10 to 80 °C with an increment of 5 and 10 °C. Each sample was mounted on an Anton Parr HTK1200 heating stage with housing, then heated to the appropriate temperature and kept for 5 min to stabilize before XRD data was collected. The XRD measurements of the VO<sub>2</sub> and W<sub>x</sub>V<sub>1-x</sub>O<sub>2</sub> thin films were analyzed using the FullProf Suite software 3.00, and the pseudo-Voigt profile function for Profile matching and Rietveld refinement were performed. The *a* and *b* lattice parameters of monoclinic and rutile VO<sub>2</sub> phases were tracked and evaluated at different temperatures using Le Bail analysis to determine the phase transition temperature. The X-ray photoelectron spectra

(XPS) were recorded on an Omicron energy analyzer (EA-125) with an Al Kα (1486.6 eV) X-ray source. Temperature-dependent resistivity measurements data were performed from 25 to 100 °C for heating and cooling using the Ossila Four-Point Probe (Ossila Ltd., Sheffield, UK).

### 3. RESULTS AND DISCUSSION

**3.1. Surface Morphology.** The SEM image analysis was initially acquired to understand the effect of doping W with VO<sub>2</sub> on the morphology and grain sizes. Figure 1 shows the top-view SEM images and particle size distribution of the VO<sub>2</sub> and different concentrations of W<sub>x</sub>V<sub>1-x</sub>O<sub>2</sub> thin films deposited on a silica substrate labeled VW-0, VW-1, VW-2, and VW-3. Noticeably, the particle sizes are uniform with irregular and spherical shapes for samples VW-0, VW-1, and VW-2. However, as the W<sup>6+</sup> ion concentration increased, the grain sizes decreased immensely for the sample VW-3. The decrease in grain size, surface porosity, and electronic structure of sample VW-3 may be attributed to the crystal lattice's energetic and kinetically disordered crystallization.<sup>18</sup> In addition, substituting the W<sup>6+</sup> ion into the VO<sub>2</sub> lattice crystal may deform the matrix's bonding lengths and coordination spheres, leading to interfacial strain and decreasing grain size. Subsequently, the VO<sub>2</sub> particle distribution on the silica substrate was evaluated using ImageJ software and SEM images. Figure 2 shows a particle size histogram fitted with Gaussian distribution curves. These analyses reveal average particle sizes of 800 ± 20, 800 ± 23, 700 ± 50, and 200 ± 17 nm for samples VW-0, VW-1, VW-2, and VW-3.

**3.2. TEM Cross Section and Crystallography Analysis of the Thin Films.** Bright-field TEM cross-sectional images of all the fabricated samples were prepared using a focused ion beam (FIB, FEI Helios G4 CX DualBeam). Figure 3a1,b1 shows bright-field cross-sectional TEM images of the samples VW-0 and VW-2 exhibiting heterostructures with average thin film thicknesses of ~0.98 and ~1.06 μm. The SAED patterns were acquired randomly from the areas circled in green, as shown in

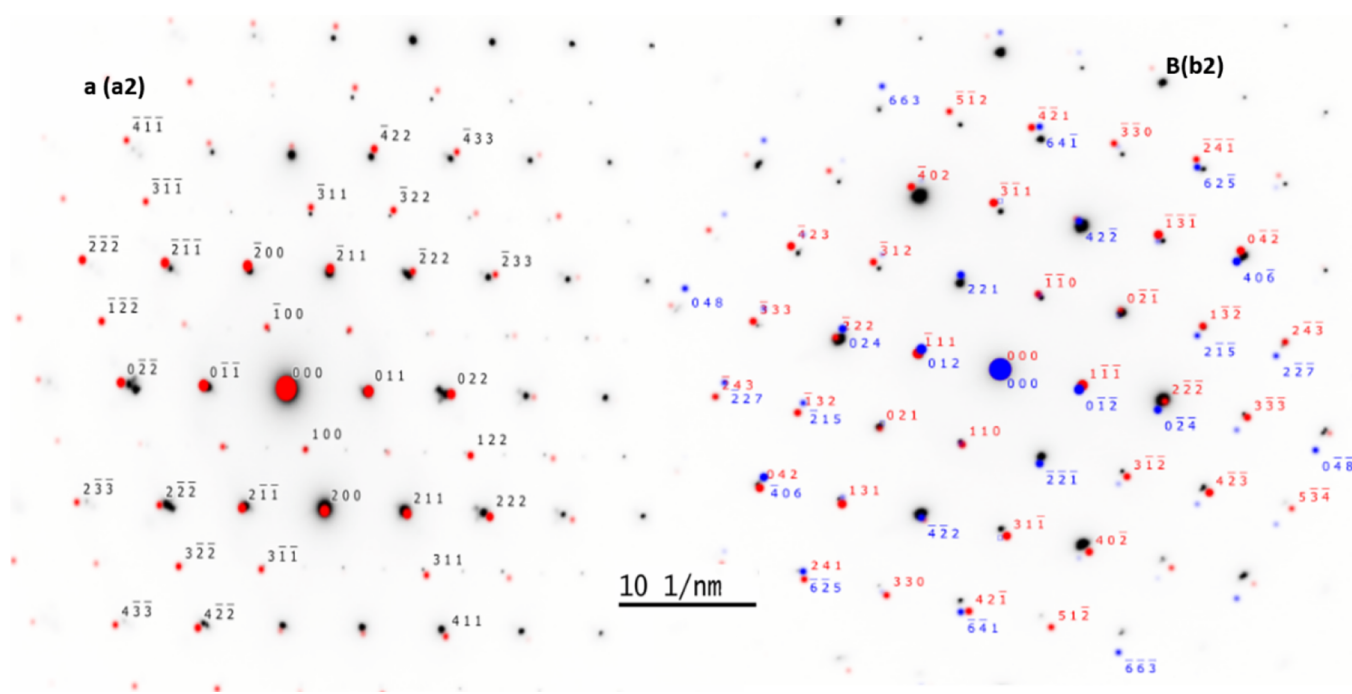


**Figure 4.** Electron diffraction patterns of the VO<sub>2</sub> matrix from the [011] plane of the VO<sub>2</sub> thin film. (a) Sample VW-0 of Figure 3a2 and (b) sample VW-2 of Figure 3b2.

Figures 3a2,a3,b2,b3. The SAED pattern depicted in Figure 3a2,a3 demonstrates the basic structural information on the monoclinic VO<sub>2</sub> (M1) phase without impurity. The SAED pattern also reveals the characteristics of long-range ordered polycrystalline structures. Furthermore, the magnified HRTEM image has interplanar spacing correlating to an out-of-plane and in-plane spacings of 0.342 and 0.171 nm, which correspond to (110) and (−211) planes of VO<sub>2</sub> (M1) as illustrated in Figure 3a4. Similarly, the SAED pattern of the sample VW-2 shows mixed monoclinic M1 and M2 phases of VO<sub>2</sub> along with interplanar spacings of 0.321 and 0.453 nm, which correspond to (110) and (−111) zone axis. To validate the crystal structure of the thin films prepared, electron diffraction patterns of samples VW-0 and VW-2 SAED were employed to determine lattice parameters using SingleCrystal software for comparison. Figure 4a shows two mirror lattice constant patterns obtained from sample VW-0, which confirms the M1 phase of the VO<sub>2</sub> polycrystalline lattice. Likewise, Figure 4b, consisting of Figure 3b2, shows the lattice constant patterns acquired from the VO<sub>2</sub> lattice along the [110] and [−111] plane axes for the M1 and M2 mixed phases indicated in red and blue.

**3.3. Structural Transformation and Stability of the M2 Phase.** Following the SEM analysis, XRD patterns of the fabricated undoped VO<sub>2</sub> and W<sub>x</sub>V<sub>1-x</sub>O<sub>2</sub> thin films were collected using a  $\theta$ – $2\theta$  scan to investigate their crystalline phases, as depicted in Figure 5. The diffraction patterns of the undoped VO<sub>2</sub> (sample VW-0) illustrate about seven prominent polycrystalline peaks centered at  $2\theta = 27.82^\circ, \sim 33.37^\circ, \sim 37.04^\circ, \sim 39.04^\circ, \sim 42.14^\circ, \sim 55.43^\circ,$  and  $\sim 57.8^\circ$ . These peaks corresponded to the following crystallographic planes (*hkl*) of (011), (−102), (200), (−112), (210), (220), and (022), with the reflection of VO<sub>2</sub> (M1) phase and crystal group of P21/c (JCPDS Card No. 72-0514).<sup>19</sup> The XRD patterns obtained for undoped VO<sub>2</sub> thin film structures are comparable to polycrystalline structures reported in the literature.<sup>1</sup> Furthermore, the XRD patterns of various concentrations of W<sup>6+</sup>-doped VO<sub>2</sub> thin film

samples exhibit additional orientation peaks at  $12.22^\circ, 15.01^\circ, 17.86^\circ, 30.13^\circ, 35.80^\circ,$  and  $45.44^\circ$  with increasing intensity as the W<sup>6+</sup> content increases. These different diffraction peaks seen in Figure 5 for samples VW-1, VW-2, and VW-3 are indexed as mixed phases of the monoclinic crystalline phase of VO<sub>2</sub>(M2) and VO<sub>2</sub>(B) with a space group C2/m, which correlate with the JCPDS 70–3131<sup>2</sup> and JCPDS Card No. 65–7960.<sup>2,20</sup> These results confirm the formation of mixed phases consisting of VO<sub>2</sub>(M1), VO<sub>2</sub>(M2), and VO<sub>2</sub>(B) phases of chemical formula W<sub>0.6</sub>V<sub>2.4</sub>O<sub>7</sub> under the current experimental condition. Figure 5b shows  $2\theta$  scan XRD diffraction patterns for VO<sub>2</sub>(M2) and VO<sub>2</sub>(M1) peaks centered at  $\sim 26.80^\circ$  (−111) and  $\sim 27.82^\circ$  (011) with the intensity of the M2 phase increasing as W<sup>6+</sup> content increases. These results indicate that the M2 phase becomes more stable and dominant over the M1 phase as the W<sup>6+</sup> content increases. This is attributed to the induced microstrain caused by substituting W<sup>6+</sup> ions into the VO<sub>2</sub> lattice structure. The XRD patterns agree with the TEM SAED patterns depicted in Figure 4a.

Furthermore, the average crystalline size, *d*, of the four different VO<sub>2</sub> films fabricated was determined employing the full-width-half-maximum (fwhm) values obtained from diffraction peaks at  $\sim 26.80^\circ$  and  $\sim 27.82^\circ$  and Debye–Scherrer equation.<sup>21</sup>

$$d = \frac{0.9\lambda}{\beta \cos \theta} \quad (1)$$

The variation in the crystallinity size at the two diffraction peaks for each sample was approximately the same. Nevertheless, the average crystalline size obtained from the Debye–Scherrer equation was <200 nm compared to the average particle size calculated from the SEM images depicted in Figure 2.

Following the Debye–Scherrer equation analysis, the microstrain distortion induced by W<sup>6+</sup> ions in VO<sub>2</sub> thin films was determined. The microstrain or strain effect plays an important

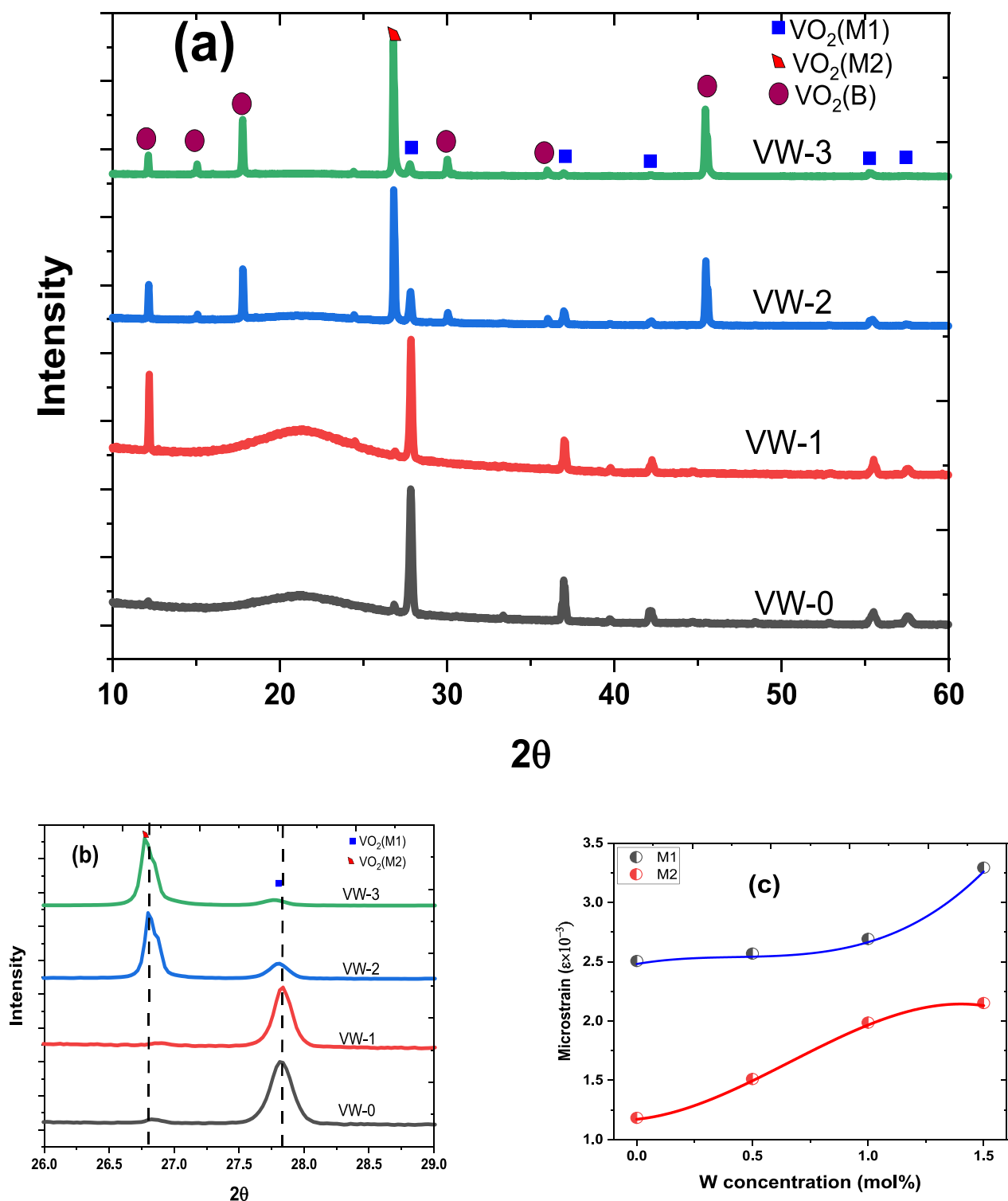


**Figure 5.** (a) XRD patterns of the undoped  $\text{VO}_2$  and different concentrations of W-doped  $\text{VO}_2$  thin films at room temperature at  $\theta$ - $2\theta$  scans showing  $\text{VO}_2(\text{M1})$ ,  $\text{VO}_2(\text{M2})$ , and  $\text{VO}_2(\text{B})$  phases, (b) XRD patterns for  $\theta$ - $2\theta$  scans ranging from  $26^\circ$  to  $29.0^\circ$ , and (c) variation of microstrain with W concentration.

role in the electrical and optical properties and transition temperatures of the  $\text{VO}_2$  thin films. Therefore, the diffraction peaks centered at  $2\theta = \sim 26.80^\circ$  (M2) and  $\sim 27.82^\circ$  (M1) were used to investigate the microstrain or strain effect by following the relationship.<sup>22</sup>

$$\varepsilon = \frac{\beta}{4 \tan \theta} \quad (2)$$

where  $\lambda$  is the wavelength of the incident X-ray beam ( $\lambda = 0.15406$  nm),  $\beta$  represents the fwhm, and  $\theta$  indicates Bragg's angle.

Figure 5c shows the effect of the microstrain through an increase in  $\text{W}^{6+}$  content-doped  $\text{VO}_2$  thin films. It was observed

that the microstrain increased slightly with  $W^{6+}$  content, which may be attributed to the defect induced by  $W^{6+}$  in the  $VO_2$  lattice structure. Thus, such an increase in microstrain may be ascribed to local structure modification of electron–electron interactions in the  $VO_2$  thin film crystal structure, resulting in stabilization of the M2 phase.<sup>23–25</sup> Furthermore, the dominating of the M2 phase over the M1 stage at higher  $W^{6+}$  content may be ascribed to the differences in visible grain orientation and breaks up of the  $V^{4+}-V^{4+}$  bonds to form new bonds such as  $V^{4+}-W^{6+}$ ,  $V^{3+}-W^{6+}$ , and  $V^{3+}-V^{4+}$ .<sup>23</sup>

**3.4. Valence States and Ratios of Vanadium.** X-ray photoelectron spectroscopy (XPS) analysis was performed to ascertain the correct electronic states of vanadium(V) and tungsten (W) in the undoped and W-doped  $VO_2$  thin films. It is well-known that the valence states of V and W can significantly affect the  $VO_2$  thin film transition temperature.<sup>26–28</sup> Figure 6

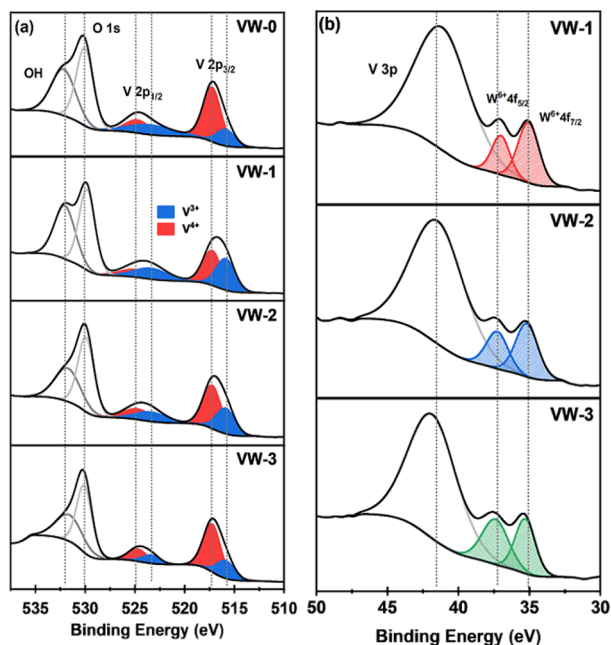


**Figure 6.** XPS spectra of pure  $VO_2$  and  $V_{1-x}W_xO_2$  thin films: (a) OH, O 1s, and V 2p and (b) V 3p and W 4f.

shows XPS spectra of pure  $VO_2$  and  $V_{1-x}W_xO_2$  thin film samples (VW-0, VW-1, VW-2, VW-3), which were deconvoluted with peak-fitting of XPS spectral of hydroxyl (OH), oxygen (O 1s), and V-2p to determine the prominent characteristics binding energies. The oxidation states of V-2p present in the thin film sample surface are composed of typical two-peak patterns of V-2p<sub>1/2</sub> and V-2p<sub>3/2</sub>, which are attributed to the spin–orbital splitting features. The binding energies with peak positions due to spin splitting feature V-2p<sub>3/2</sub>, which occurred at  $\sim 515$  and  $\sim 517$  eV, are ascribed to  $V^{3+}$  and  $V^{4+}$  oxidation states of V species in pure and doped thin films,<sup>29</sup> respectively. Similarly, the spectral feature V-2p<sub>1/2</sub> has corresponding binding energy peaks at  $\sim 523$  and  $\sim 524$  eV, belonging to  $V^{3+}$  and  $V^{4+}$  oxidation states.<sup>29</sup> According to Kurmaev et al.,<sup>30</sup> the presence of  $V^{3+}$  valence states in all the thin film samples prepared may be attributed to the high-temperature environment used during sample fabrication and oxygen vacancies, leading to thin film charge localization and surface segregation.

Meanwhile, the XPS spectral peak of O 1s appeared at  $\sim 529$  eV, which can be assigned to  $O^{2-}$  in the V–O binding, while the

OH peak occurred at  $\sim 531$  eV. Liu et al.<sup>27</sup> reported that the presence of oxygen vacancies in the crystal lattice had a great influence on the  $VO_2$  thin film transition temperature, electrical and optical properties. The spectral feature that emerged at 531.4 eV corresponds to the OH concentration, which decreases with an increase in tungsten doping concentration. The presence of the OH content on the surface of the  $VO_2$  thin film may be ascribed to the environment and surface water adsorption. XPS spectra depicted in Figure 6b show W 4f photoelectron spectra of samples VW-1, VW-2, and VW-3 with the peaks located at 35.07 and 37.13 eV confirming the existence of W 4f<sub>7/2</sub> and W 4f<sub>5/2</sub> induced by  $W^{6+}$  ions. The binding energy peak at 41.5 eV is ascribed to V 3p.

The influence of the W content on the V valence states was investigated by fitting the area under the curves of  $V^{3+}$  and  $V^{4+}$ . Figure 7 compares the  $V^{3+}$  and  $V^{4+}$  valence state content

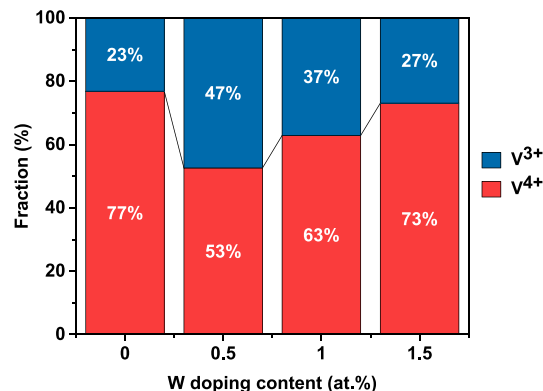


**Figure 7.** Average fraction of  $V^{3+}$  and  $V^{4+}$  contents in the thin films prepared as a function of W content.

percentage ratios as a function of W doping concentration. The proportion of  $V^{3+}$  decreases, and  $V^{4+}$  increases with increasing W concentration, which confirms the stabilization of the  $V^{4+}$  state. The chemical composition of each sample prepared was determined to be  $VO_{1.69}$ ,  $VO_{1.47}$ ,  $VO_{1.21}$ , and  $VO_{1.14}$  for samples VW-0, VW-1, VW-2, and VW-3. This demonstrates that oxygen deficiency increases by increasing the W content under the same fabrication condition.

**3.5. Lattice Parameter Distortions Drove by Temperature-Dependent XRD Data.** Following the observed temperature-related changes to the physical and optical properties, we investigated the  $VO_2$  and  $W^{6+}$  doped  $VO_2$  thin film microstructures by performing temperature-dependent XRD measurements. This provides a clearer quantitative understanding of how the  $W^{6+}$  content affects the  $VO_2$  thin film crystal structure and lattice parameters during the MIT mechanism from the M1  $\rightarrow$  M2  $\rightarrow$  R and M1  $\rightarrow$  R transition. Figure 8a illustrates  $2\theta$  scans temperature-dependent structural phase transition of the  $VO_2$  and  $W^{6+}$ -doped  $VO_2$  films, with  $2\theta$  between  $27.4^\circ$  and  $28.4^\circ$  and at temperatures ranging from 25 to  $85^\circ\text{C}$  covering the range over which the physical properties are changing. The diffraction peak of the  $VO_2$  (M1) (011) phase of the thin films at a low-temperature range undergoes a change to the R(110) phase at a high temperature (JCPDS file 01–079–1655). In Figure 8a, two different transition peaks emerged from samples VW-0 and VW-1, denoted by M1(011) peaks at  $27.84^\circ$  and R(110) peaks at  $27.68^\circ$ , transitioning from room temperature ( $25^\circ\text{C}$ ) to a high temperature of  $85^\circ\text{C}$ , respectively. As the temperature increases from 25 to  $60^\circ\text{C}$  and from 25 to  $50^\circ\text{C}$

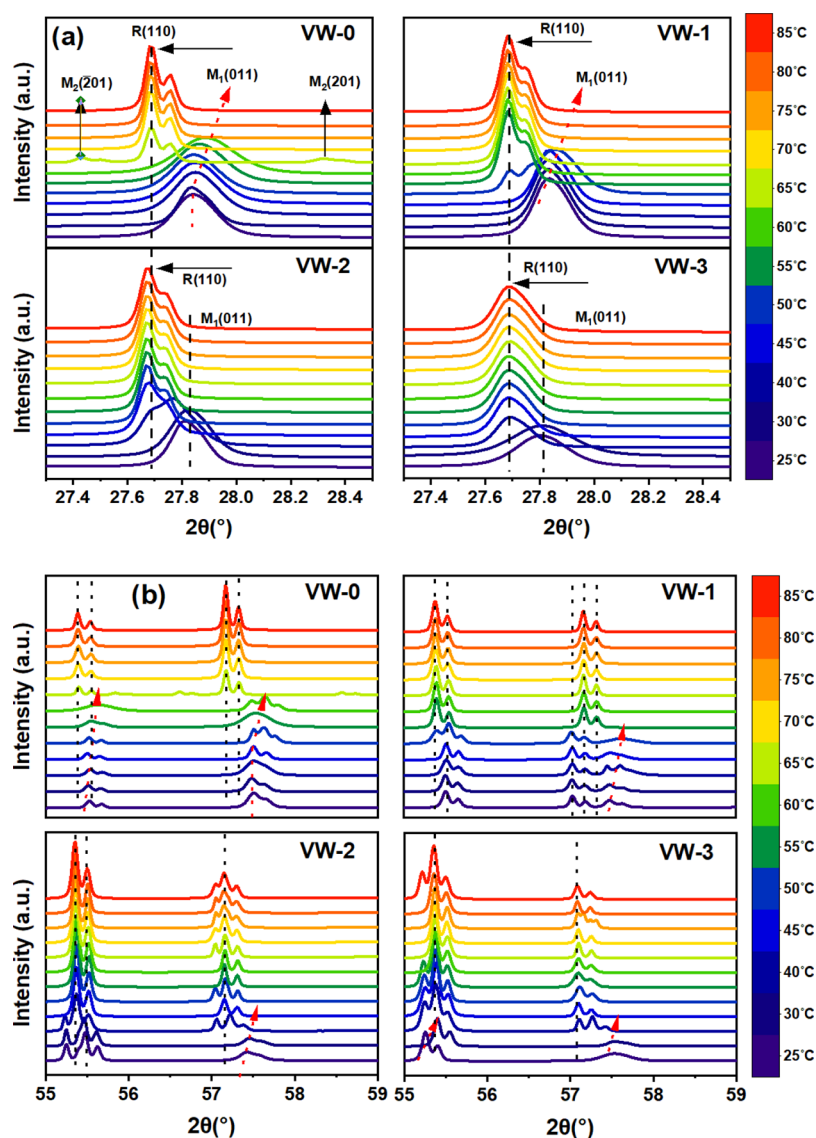


**Figure 8.** Temperature-dependent XRD patterns for samples VW-0, VW-1, VW-2, and VW-3 with heating temperatures ranging from 25 to 85 °C exhibiting phase-transition related to changes in the diffraction patterns are visible: (a) selected  $2\theta$  range of 27.4° to 28.4° and (b) selected  $2\theta$  range of 55° to 59°.

for samples VW-0 and VW-1, the M1 peak is shifted to the larger angle, whereas peak R(110) arises from moving between 65 and 60 °C, and continues to stabilize further above 80 °C. At the elevated temperature of around 65 °C, we observe three diffraction peaks occurring at 27.43°, 27.68°, and 28.32° labeled as M2(-201), R(110), and M2(201), which provide clear evidence for the coexistence of multiple phases in sample VW-0.<sup>31</sup> Similarly, sample VW-1 reveals three diffraction peaks identical to those of sample VW-0. The M2(201) intermediate structure may be ascribed to different mechanisms, such as strain and stress at the thin film interface, doping with W<sup>6+</sup> and defects on the thin film.<sup>24</sup> In the case of sample VW-3, two peaks at  $2\theta$  of 27.65° and 27.84° can be attributed to the monoclinic M1 phase at a lower temperature in the presence of the metallic R phase at a higher temperature.

Furthermore, Figure 8b shows XRD patterns between  $2\theta$  of ~55° and ~59° obtained while heating the VO<sub>2</sub> and W<sup>6+</sup>-doped VO<sub>2</sub> thin film samples. The VO<sub>2</sub> diffraction peaks occur at ~55.43° (220) and ~57.8° (022) and are also shifted to the higher angle at the low-temperature range, corresponding to the

monoclinic M1 phase. At the elevated temperature, the XRD patterns move to lower angles, indicating a phase transition from monoclinic M1 to the metallic R phase as a result of the heating process. Meanwhile, shifting the M1 structural phase to a higher  $2\theta$  angle during heating results from the strain induced at the thin film and silica substrate interface, leading to a mesoscopic phase separation. These results demonstrate that the various diffraction peaks seen in the VO<sub>2</sub> and W<sup>6+</sup>-doped VO<sub>2</sub> thin films fabricated by fs-PLD can be used to predict VO<sub>2</sub> (M1) phase transition temperature accurately.

The local crystalline lattice parameters  $a$  and  $b$  were calculated using FullProf software to help shed light on the subsequent measured behavior. The trend of  $a$  and  $b$  lattice parameters as a function of temperature was obtained by using temperature dependent XRD patterns in the range of  $2\theta$  from 26° to 60°. Figure 9 illustrates a plot of the variation of these lattice parameters  $a$  and  $b$  with temperature for samples VW-0, VW-1, VW-2, and VW-3 exhibiting hysteresis properties, respectively. A-lattice ( $b$ -lattice) gradually shifted to a lower (higher) value as the temperature increased, with a clear distinction between the

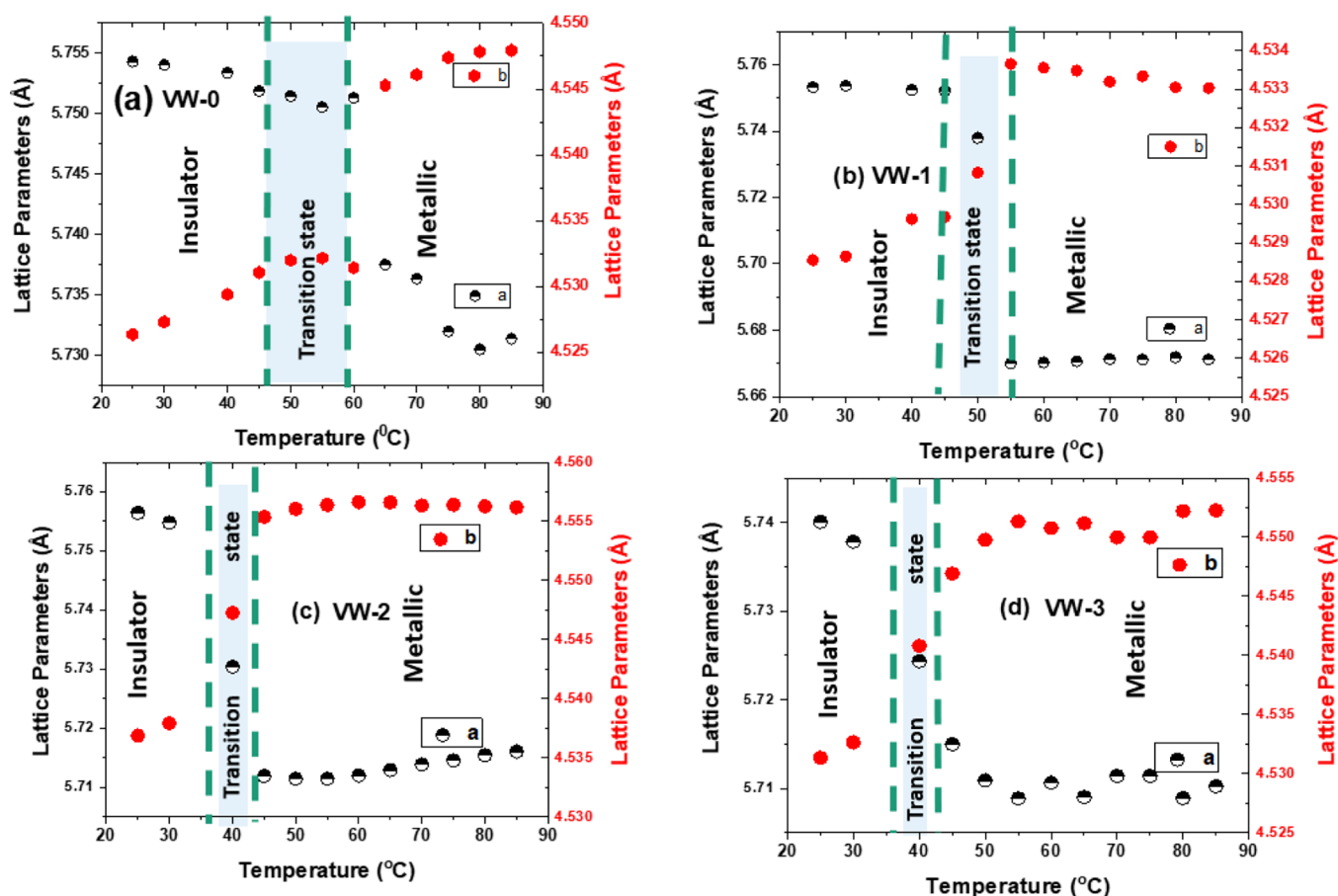


**Figure 9.** Lattice parameters  $a$  and  $b$  of  $\text{VO}_2$  and  $\text{W-VO}_2$  thin films as function temperature (a) VW-0, (b) VW-1, (c) VW-2 and (d) VW-3.

insulator state (M1) and metallic state (R). This trend indicates that  $a$ -lattice and  $b$ -lattice parameters are associated with contraction and expansion in the  $\text{VO}_2$  thin film samples during heating from room temperature up to  $85^\circ\text{C}$ . The range of the  $a$  and  $b$  lattice parameters seen in samples VW-0, VW-1, VW-2, and VW-3 are in good agreement with the observations by Liu et al.,<sup>15</sup> who deposited  $\text{VO}_2$  thin films on (0001)- $\text{Al}_2\text{O}_3$  single-crystal substrates using RF magnetron sputtering. Similarly, the trends of the  $a$  and  $b$  lattice parameters as a function of temperatures are comparable to our results.

The MIT transition temperatures of the pure  $\text{VO}_2$  and  $\text{W}^{6+}$ -doped  $\text{VO}_2$  thin films were evaluated by employing the first derivative logarithms of lattice parameters  $a$  and  $b$  for the temperature {i.e.  $d[\log(a&b)]/dT$ }. Figure 10a–d shows the plots of  $d[\log(a&b)]/dT$  versus temperature, which was fitted with the Lorentz equation using OriginPro software. The phase transition temperatures ( $T_t$ ) of the thin films were determined using the expression  $T_t = \frac{1}{2}(T_a + T_b)$ . Table 1 below summarizes the phase transition temperatures of various samples during the contraction and expansion of the  $a$  and  $b$  parameters. It is observed that the average transition temperature of samples VW series decreases from  $\sim 66$  to  $38^\circ\text{C}$  as the  $\text{W}^{6+}$  concentration increases from 0.0 to 1.5 wt %. Thus, such a decrease in phase transition is mostly attributed to an increase in  $\text{W}^{6+}$  doping concentration, induced microstrain and particle sizes, as illustrated in Figure 5c. In addition, the  $\text{VO}_2$  thin film induces compressive strain along the  $a$  axis, which can lower the transition temperature to near room temperature, as shown in Figure 10a–d. The structural phase transition temperatures

obtained from samples VW-0, VW-1, VW-2, and VW-3 correlate with the results by Chen et al.,<sup>5</sup> where they synthesized  $\text{W}^{6+}$ -doped  $\text{VO}_2$  thin film samples with  $\text{W}^{6+}$  concentrations of 0%, 0.5%, 1%, 1.5%, and 2% using a cosputtering method and followed by post-annealing. They measured temperature-dependent transmission in the near-infrared region and reported tuning the phase transition temperatures from  $64.3$  to  $36.5^\circ\text{C}$ . Similarly, Rajeswaran et al.<sup>24</sup> fabricated polycrystalline  $\text{W}_x\text{V}_{1-x}\text{O}_2$  thin films using ultrasonic nebulized spray pyrolysis of aqueous combustion mixtures, with  $\text{W}^{6+}$  content varying between  $x = 0.2$  and  $2.0$  at. %. The authors reported that transition temperatures decreased from  $68$  to  $25^\circ\text{C}$  by doping the  $\text{VO}_2$  with  $2.0$  at% of  $\text{W}^{6+}$  and measuring the temperature-dependent resistance of the thin films. According to these literature results, the variation in the transition temperature is affected by the nature of the  $\text{VO}_2$  thin film phases, such as M1, M2, T, and R, together with surface morphology and orientation of the grains and their grain boundaries.<sup>32</sup> According to Tang et al.<sup>23</sup> and He et al.<sup>33</sup> the loss of direct bonding between the  $\text{V}^{4+}$ – $\text{V}^{4+}$  homopolar and  $\text{V}^{3+}$ – $\text{V}^{4+}$  heteropolar bonds by doping  $\text{W}^{6+}$  with  $\text{VO}_2$  destabilizes the  $\text{VO}_2$  semiconducting phase to lower the phase transition temperature. In addition, a high doping concentration of the  $\text{W}^{6+}$  valence state may lead to a boost of free-electron concentration and then lead to a transition temperature drop.<sup>34</sup> It is also important to note that the transition temperatures obtained from our study are comparable to temperature-dependent resistivity transition temperatures of similar doping concentrations reported elsewhere.<sup>35,36</sup>

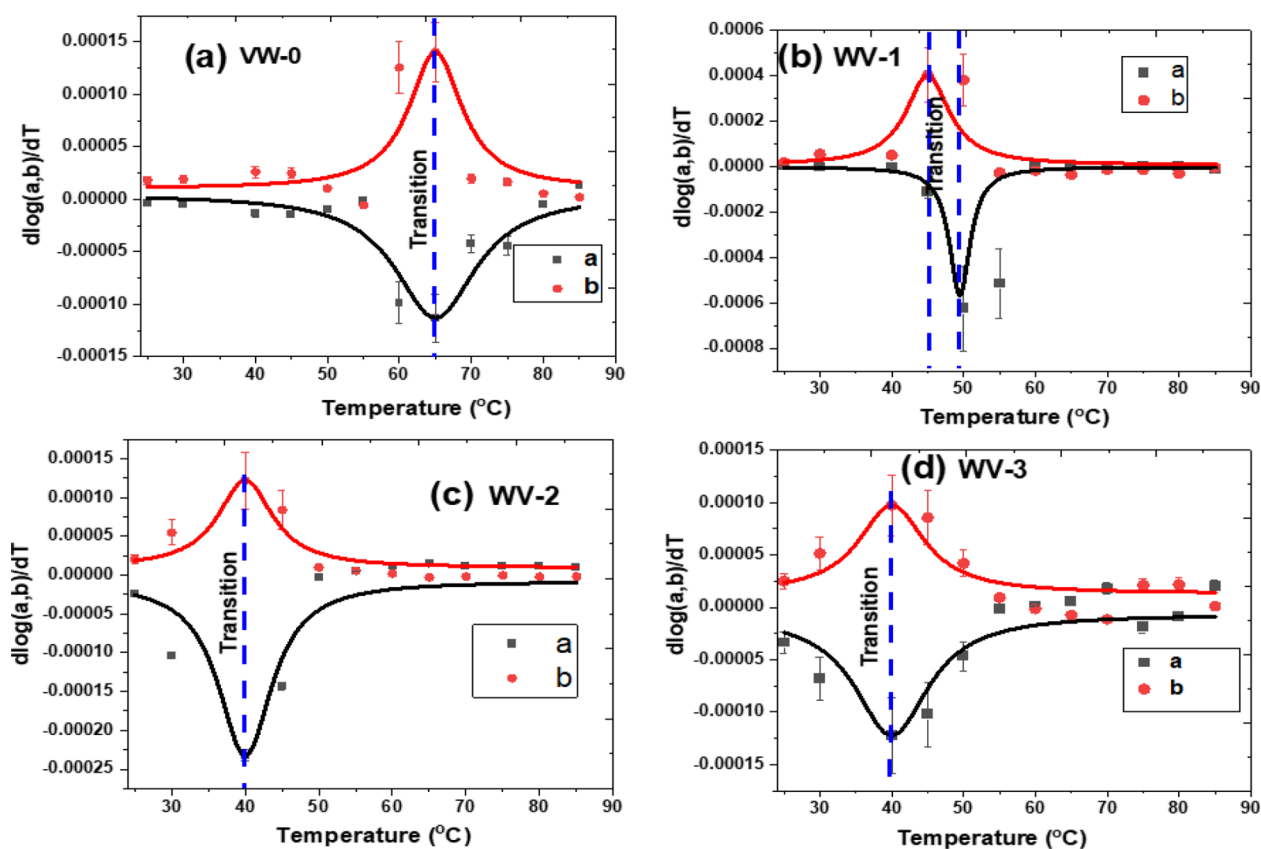


**Figure 10.** First derivative of the  $\log_{10}(a \text{ \& } b)$  lattice parameters) as a function of temperature fitted with Lorentz equation: (a) VW-0, (b) VW-1, (c) VW-2, and (d) VW-3.

**Table 1.** *a* and *b* Lattice Parameters Transition Temperatures and Average Transition Temperature of the As-Deposited  $\text{VO}_2$  and  $\text{W}^{6+}$ -Doped  $\text{VO}_2$  Thin Films

sample ID	transition temp. for a-lattice ( $^{\circ}\text{C}$ ) ( $T_a$ )	transition temp. for b-lattice ( $^{\circ}\text{C}$ ) ( $T_b$ )	average transition temperature ( $^{\circ}\text{C}$ ) ( $T_t$ )
VW-0	$65.3 \pm 4.4$	$65.7 \pm 5.8$	$65.5 \pm 5.1$
VW-1	$45.7 \pm 3.6$	$49.5 \pm 4.3$	$47.6 \pm 3.9$
VW-2	$40.9 \pm 2.7$	$39.9 \pm 1.6$	$40.4 \pm 2.2$
VW-3	$38.4 \pm 1.8$	$38.4 \pm 3.8$	$38.4 \pm 2.8$

**3.6. Temperature-Dependent Electrical Resistivity of  $\text{VO}_2$  Phase Transition.** The temperature-dependent resistivities of the thin films prepared were investigated by using a four-point probe purchased from Ossila Ltd. The electrical resistivity was recorded from room temperature to  $100^{\circ}\text{C}$  for comparison with the temperature-dependent XRD results illustrated in Figures 9 and 10. Figure 11 shows the results of temperature-dependent electrical resistivity plots during the heating and cooling cycles of samples VW-0 and VW-3. The thin film sample VW-0 exhibits a metal-to-insulator transition with 2 orders of magnitude change in resistivity switched compared to sample VW-3, which has a resistivity change by a single order. The semiconductor metal-to-insulator transition was determined utilizing the first derivative of the resistivity with respect to temperature [ i.e.,  $d[\log(\rho)]/dT$ ]. The resulting curves are shown in Figure 12a,b for samples VW-0 and VW-3, which are fitted with Gaussian functions with minima corresponding to heating,  $T_h$ , and cooling,  $T_c$  phase transition temperature. Similar temperature-dependent resistivity measurements were performed for samples VW-1 and VW-2 to determine the

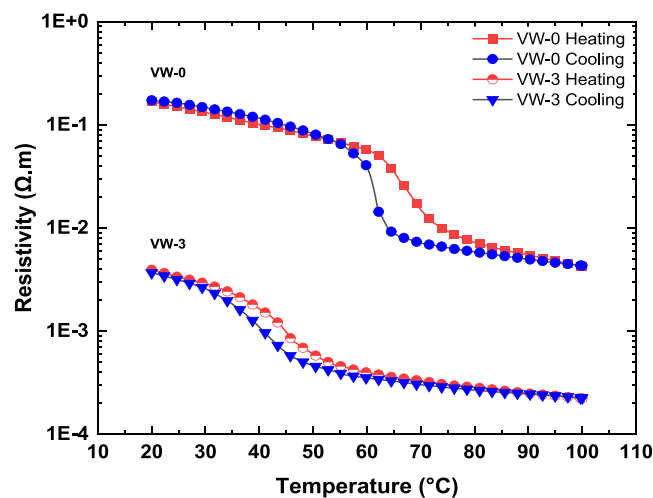


**Figure 11.** Resistivity as a function of temperature curve of samples VW-0 and VW-3.

transition temperature, which is not shown (to be published later). Table 2 represents the average transition temperatures obtained from temperature-dependent resistivity measurements, which are in agreement with those reported from the *a* and *b* lattice parameters presented in section 3.5. The average MIT decreases with an increasing doping concentration of W.

## 4. CONCLUSIONS

A high repetition rate femtosecond-PLD approach has been used to deposit thicker  $\text{VO}_2$  and  $\text{W}^{6+}$  doped  $\text{VO}_2$  on silica

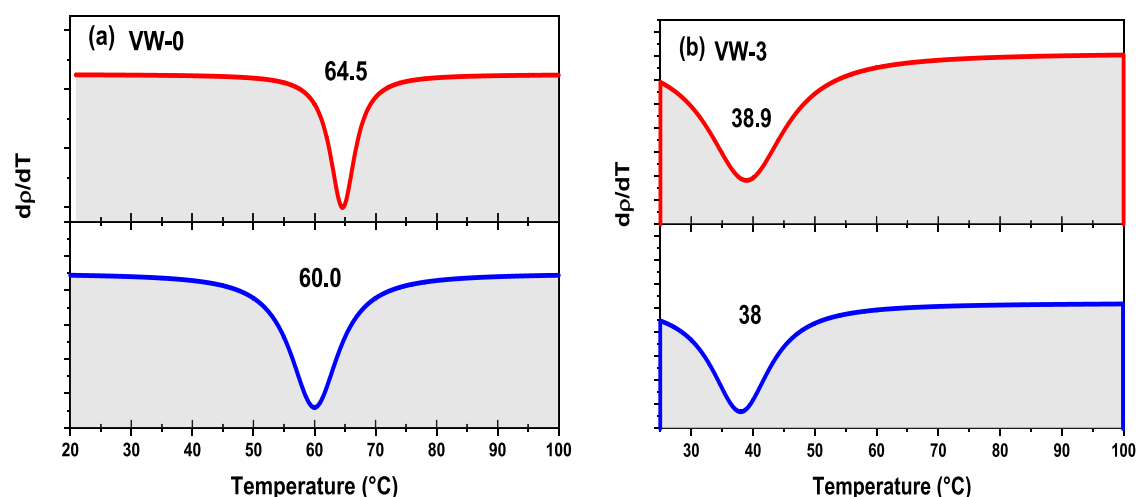


Figure 12. Gaussian fitting of the first derivative of the resistivity with respect to temperature vs temperature for samples (a) VW-0 and (b) VW-3.

Table 2. Average Transition Temperature Obtained from Heating and Cooling Temperature-Dependent Resistivity Measurements for Undoped VO<sub>2</sub> and All W-Doped VO<sub>2</sub> Thin Films

sample ID	transition temp. for heating (°C) [T <sub>h</sub> ]	transition temp. for cooling (°C) [T <sub>c</sub> ]	average transition temperature (°C) T <sub>i</sub> = $\frac{1}{2}(T_h + T_c)$
VW-0	64.5 ± 2.7	60.0 ± 2.5	62.3 ± 2.6
VW-1	46.8 ± 3.2	47.8 ± 3.3	47.3 ± 3.2
VW-2	41.0 ± 1.5	42.0 ± 2.3	41.5 ± 1.9
VW-3	38.9 ± 1.3	38.0 ± 2.7	38.5 ± 2.0

substrates. The thin films' surface morphology, particle size, and crystal orientation were confirmed using SEM and room temperature XRD measurements. The XRD measurements revealed mixed phases of the highly dense polycrystalline monoclinic crystalline structures of VO<sub>2</sub>(M1) and (M2) for W<sup>6+</sup>-doped VO<sub>2</sub> thin film samples. With increasing W<sup>6+</sup> concentration, the VO<sub>2</sub>(M2) phase becomes dominant and stable and exists together with VO<sub>2</sub>(M1) and VO<sub>2</sub>(B) phases; however, it suppresses the XRD peak intensity of the VO<sub>2</sub>(M1) phase due to the W<sup>6+</sup> content. Thus, this is ascribed to the strain induced by doping the VO<sub>2</sub> with the W<sup>6+</sup> ions and the uniformly distributed W<sup>6+</sup> in the VO<sub>2</sub> matrix, favoring the VO<sub>2</sub>(M2) phase formation instead of the VO<sub>2</sub>(M1) phase. The temperature-dependent measurements showed a remarkably sharp change in the *a* and *b* lattice parameters from room temperature to a high temperature of about 85 °C. These lattice parameter changes result in a sharp decrease at the MIT temperature, corresponding to the structural phase transformation from monoclinic M1 to the metallic R phase. The phase transition temperature decreases from ~66 to 38 °C when increasing the W<sup>6+</sup> concentration. This study demonstrates the nature of the changes in the temperature-dependent lattice parameters, offering the potential to understand and more accurately predict the structural phase transitions of VO<sub>2</sub> and W<sup>6+</sup>-doped VO<sub>2</sub> thin films, which affect the resistivity and optical transmission behavior as a function of temperature.

## AUTHOR INFORMATION

### Corresponding Author

Eric Kumi Barimah – School of Chemical and Process Engineering, University of Leeds, Leeds LS2 9JT, U.K.;

orcid.org/0000-0003-4841-9866; Email: e.kumi-barimah@leeds.ac.uk

## Authors

Artisupa Boontan – School of Chemical and Process Engineering, University of Leeds, Leeds LS2 9JT, U.K.

Paul Steenson – School of Electronic and Electrical Engineering, University of Leeds, Leeds LS2 9JT, U.K.

Gin Jose – School of Chemical and Process Engineering, University of Leeds, Leeds LS2 9JT, U.K.

Complete contact information is available at:

<https://pubs.acs.org/10.1021/acsami.3c11484>

## Notes

The authors declare no competing financial interest.

## ACKNOWLEDGMENTS

This work was financially supported by the Engineering and Physical Science Research Council (EPSRC) through the research grants EP/M015165/1, EP/M022854/1, and EP/T004711/1. In addition, the first author acknowledges the financial support from the Royal Thai Government Scholarship for her doctoral study at the University of Leeds. We also thank Dr. Zabeada Aslam and Dr. Jake Sheriff at the Leeds Electron Microscopy and Spectroscopy (LEMAS) Centre, University of Leeds and Newcastle University for their support in carrying out the TEM cross-section and XPS measurements.

## REFERENCES

- Zhang, Y.; Xiong, W.; Chen, W.; Zheng, Y. Recent Progress on Vanadium Dioxide Nanostructures and Devices: Fabrication, Properties, Applications and Perspectives. *Nanomaterials* **2021**, *11* (2), 338.
- Srivastava, A.; Rotella, H.; Saha, S.; Pal, B.; Kalon, G.; Mathew, S.; Motapothula, M.; Dykas, M.; Yang, P.; Okunishi, E.; Sarma, D. D.; Venkatesan, T. Selective Growth of Single Phase VO<sub>2</sub> (A, B, and M) Polymorph Thin Films. *APL Mater.* **2015**, *3* (2), No. 026101.
- Kumi-Barimah, E.; Anagnostou, D. E.; Jose, G. Phase Changeable Vanadium Dioxide (VO<sub>2</sub>) Thin Films Grown from Vanadium Pentoxide (V<sub>2</sub>O<sub>5</sub>) Using Femtosecond Pulsed Laser Deposition. *AIP Adv.* **2020**, *10* (6), No. 065225.
- Liu, K.; Lee, S.; Yang, S.; Delaire, O.; Wu, J. Recent Progresses on Physics and Applications of Vanadium Dioxide. *Mater. Today* **2018**, *21* (8), 875–896.
- Chen, X.; Wu, M.; Liu, X.; Wang, D.; Liu, F.; Chen, Y.; Yi, F.; Huang, W.; Wang, S. Tuning the Doping Ratio and Phase Transition

- Temperature of VO<sub>2</sub> Thin Film by Dual-Target Co-Sputtering. *Nanomaterials* **2019**, *9* (6), 834.
- (6) Andrews, K.; Kaye, A. B. Controlled Tungsten Doping of Vanadium Dioxide Grown through Alternating-Target Pulsed Laser Deposition. *Mater. Res. Express* **2019**, *6* (5), No. 056402.
- (7) Li, S.-Y.; Niklasson, G. A.; Granqvist, C. G. Thermo-chromic Undoped and Mg-Doped VO<sub>2</sub> Thin Films and Nanoparticles: Optical Properties and Performance Limits for Energy Efficient Windows. *J. Appl. Phys.* **2014**, *115* (5), No. 053513.
- (8) Brown, B. L.; Lee, M.; Clem, P. G.; Nordquist, C. D.; Jordan, T. S.; Wolfley, S. L.; Leonhardt, D.; Edney, C.; Custer, J. A. Electrical and Optical Characterization of the Metal-Insulator Transition Temperature in Cr-Doped VO<sub>2</sub> Thin Films. *J. Appl. Phys.* **2013**, *113* (17), No. 173704.
- (9) Wang, S.; Wei, W.; Huang, T.; Yuan, M.; Yang, Y.; Yang, W.; Zhang, R.; Zhang, T.; Chen, Z.; Chen, X.; Shen, G.; Dai, N. Al-Doping-Induced VO<sub>2</sub> (B) Phase in VO<sub>2</sub> (M) Toward Smart Optical Thin Films with Modulated  $\Delta T_{\text{vis}}$  and  $\Delta T_c$ . *Adv. Eng. Mater.* **2019**, *21* (12), No. 1900947.
- (10) Goodenough, J. B. The Two Components of the Crystallographic Transition in VO<sub>2</sub>. *J. Solid State Chem.* **1971**, *3* (4), 490–500.
- (11) Chen, B.; Yang, D.; Charpentier, P. A.; Zeman, M. Al<sub>3+</sub>-Doped Vanadium Dioxide Thin Films Deposited by PLD. *Sol. Energy Mater. Sol. Cells* **2009**, *93* (9), 1550–1554.
- (12) Soltani, M.; Chaker, M.; Haddad, E.; Kruzelecky, R. V.; Nikanpour, D. Optical Switching of Vanadium Dioxide Thin Films Deposited by Reactive Pulsed Laser Deposition. *Journal of Vacuum Science & Technology A: Vacuum, Surfaces, and Films* **2004**, *22* (3), 859.
- (13) Burkhardt, W.; Christmann, T.; Franke, S.; Kriegseis, W.; Meister, D.; Meyer, B. K.; Niessner, W.; Schalch, D.; Scharmann, A. Tungsten and Fluorine Co-Doping of VO<sub>2</sub> Films. *Thin Solid Films* **2002**, *402* (1–2), 226–231.
- (14) Manning, T. D.; Parkin, I. P.; Pemble, M. E.; Sheel, D.; Vernardou, D. Intelligent Window Coatings: Atmospheric Pressure Chemical Vapor Deposition of Tungsten-Doped Vanadium Dioxide. *Chem. Mater.* **2004**, *16* (4), 744–749.
- (15) Liu, Y.; Wang, C.; Huang, W.; Wang, S.; Qiu, H.; Ge, W.; Chen, M.; Zhang, H.; Gu, Y.; Zhang, X.; Li, X.; Gao, X.; Yang, Y. Unraveling Structural Phase Transformation by Simultaneously Determining the Lattice Constants and Mismatch Angle in VO<sub>2</sub>/Al<sub>2</sub>O<sub>3</sub> Epitaxial Thin Films. *Front Mater.* **2022**, *9*, No. 866468, DOI: 10.3389/fmats.2022.866468.
- (16) Qiu, H.; Yang, M.; Dong, Y.; Xu, H.; Hong, B.; Gu, Y.; Yang, Y.; Zou, C.; Luo, Z.; Gao, C. The Tetragonal-like to Rutile Structural Phase Transition in Epitaxial VO<sub>2</sub>/TiO<sub>2</sub> (001) Thick Films. *New J. Phys.* **2015**, *17* (11), No. 113016.
- (17) Kumi-Barimah, E.; Boontan, A.; Steenson, D. P.; Jose, G. Infrared Optical Properties Modulation of VO<sub>2</sub> Thin Film Fabricated by Ultrafast Pulsed Laser Deposition for Thermo-chromic Smart Window Applications. *Sci. Rep.* **2022**, *12* (1), 11421.
- (18) Chang, Q.; Wang, D.; Zhao, Z.; Ling, C.; Wang, C.; Jin, H.; Li, J. Size-Controllable M-Phase VO<sub>2</sub> Nanocrystals for Flexible Thermo-chromic Energy-Saving Windows. *ACS Appl. Nano Mater.* **2021**, *4* (7), 6778–6785.
- (19) Basyooni, M. A.; Al-Dossari, M.; Zaki, S. E.; Eker, Y. R.; Yilmaz, M.; Shaban, M. Tuning the Metal-Insulator Transition Properties of VO<sub>2</sub> Thin Films with the Synergistic Combination of Oxygen Vacancies, Strain Engineering, and Tungsten Doping. *Nanomaterials* **2022**, *12* (9), 1470.
- (20) Zhang, Y.; Tan, X.; Meng, C. The Influence of VO<sub>2</sub> (B) Nanobelts on Thermal Decomposition of Ammonium Perchlorate. *Materials Science-Poland* **2015**, *33* (3), 560–565.
- (21) Ojha, P. K.; Mishra, S. K. Synthesis & Characterization of Nanostructure VO<sub>2</sub> Thin Film. *J. Phys. Conf Ser.* **2021**, *2070* (1), No. 012098.
- (22) Pang, Y.; Liu, Y.; Zhang, X.; Gao, M.; Pan, H. Role of Particle Size, Grain Size, Microstrain and Lattice Distortion in Improved Dehydrogenation Properties of the Ball-Milled Mg(AlH<sub>4</sub>)<sub>2</sub>. *Int. J. Hydrogen Energy* **2013**, *38* (3), 1460–1468.
- (23) Tang, C.; Georgopoulos, P.; Fine, M. E.; Cohen, J. B.; Nygren, M.; Knapp, G. S.; Aldred, A. Local Atomic and Electronic Arrangements in W<sub>x</sub>V<sub>1-x</sub>O<sub>2</sub>. *Phys. Rev. B* **1985**, *31* (2), 1000–1011.
- (24) Rajeswaran, B.; Umarji, A. M. Effect of W Addition on the Electrical Switching of VO<sub>2</sub> Thin Films. *AIP Adv.* **2016**, *6* (3), No. 035215.
- (25) Galy, J.; Míehe, G. Ab Initio Structures of (M<sub>2</sub>) and (M<sub>3</sub>) VO<sub>2</sub> High Pressure Phases. *Solid State Sci.* **1999**, *1* (6), 433–448.
- (26) Zhao, X.; Yan, Y.; Mao, L.; Fu, M.; Zhao, H.; Sun, L.; Xiao, Y.; Dong, G. A Relationship between the V<sup>4+</sup>/V<sup>5+</sup> Ratio and the Surface Dispersion, Surface Acidity, and Redox Performance of V<sub>2</sub>O<sub>5</sub>-WO<sub>3</sub>/TiO<sub>2</sub> SCR Catalysts. *RSC Adv.* **2018**, *8* (54), 31081–31093.
- (27) Liu, H.; Wan, D.; Ishaq, A.; Chen, L.; Guo, B.; Shi, S.; Luo, H.; Gao, Y. Sputtering Deposition of Sandwich-Structured V<sub>2</sub>O<sub>5</sub>/Metal (V, W)/V<sub>2</sub>O<sub>5</sub> Multilayers for the Preparation of High-Performance Thermally Sensitive VO<sub>2</sub> Thin Films with Selectivity of VO<sub>2</sub> (B) and VO<sub>2</sub> (M) Polymorph. *ACS Appl. Mater. Interfaces* **2016**, *8* (12), 7884–7890.
- (28) Victor, J. L.; Marcel, C.; Sauques, L.; Labrugère, C.; Amiard, F.; Gibaud, A.; Rougier, A. From Multilayers to V<sub>1-x</sub>W<sub>x</sub>O<sub>2</sub>± $\delta$  Films Elaborated by Magnetron Sputtering for Decreasing Thermo-chromic Transition Temperature. *J. Alloys Compd.* **2021**, *858*, No. 157658.
- (29) Rajeswaran, B.; Pradhan, J. K.; Anantha Ramakrishna, S.; Umarji, A. M. Thermo-chromic VO<sub>2</sub> Thin Films on ITO-Coated Glass Substrates for Broadband High Absorption at Infra-Red Frequencies. *J. Appl. Phys.* **2017**, *122* (16), No. 163107, DOI: 10.1063/1.5008730.
- (30) Kurmaev, E. Z.; Cherkashenko, V. M.; Yarmoshenko, Y. M.; Bartkowski, S.; Postnikov, A. V.; Neumann, M.; Duda, L.; Guo, J. H.; Nordgren, J.; Perelyaev, V. A.; Reichelt, W. Electronic Structure of VO<sub>2</sub> Studied by X-Ray Photoelectron and x-Ray Emission Spectroscopies. *J. Phys.: Condens. Matter* **1998**, *10*, 4081.
- (31) Nishikawa, K.; Yoshimura, M.; Watanabe, Y. Phase Transition Behavior in Nanostructured VO<sub>2</sub> with M<sub>1</sub>, M<sub>2</sub>, and R Phases Observed via Temperature-Dependent XRD Measurements. *Journal of Vacuum Science & Technology A* **2022**, *40* (3), No. 033401.
- (32) Appavoo, K.; Lei, D. Y.; Sonnefraud, Y.; Wang, B.; Pantelides, S. T.; Maier, S. A.; Haglund, R. F. Role of Defects in the Phase Transition of VO<sub>2</sub> Nanoparticles Probed by Plasmon Resonance Spectroscopy. *Nano Lett.* **2012**, *12* (2), 780–786.
- (33) He, X.; Zeng, Y.; Xu, X.; Gu, C.; Chen, F.; Wu, B.; Wang, C.; Xing, H.; Chen, X.; Chu, J. Orbital Change Manipulation Metal-Insulator Transition Temperature in W-Doped VO<sub>2</sub>. *Phys. Chem. Chem. Phys.* **2015**, *17* (17), 11638–11646.
- (34) Li, W.; Ji, S.; Li, Y.; Huang, A.; Luo, H.; Jin, P. Synthesis of VO<sub>2</sub> Nanoparticles by a Hydrothermal-Assisted Homogeneous Precipitation Approach for Thermo-chromic Applications. *RSC Adv.* **2014**, *4* (25), 13026–13033.
- (35) Majid, S. S.; Sahu, S. R.; Ahad, A.; Dey, K.; Gautam, K.; Rahman, F.; Behera, P.; Deshpande, U.; Sathe, V. G.; Shukla, D. K. Role of V-V Dimerization in the Insulator-Metal Transition and Optical Transmittance of Pure and Doped VO<sub>2</sub> Thin Films. *Phys. Rev. B* **2020**, *101* (1), No. 014108.
- (36) Paik, T.; Hong, S.-H.; Gaulling, E. A.; Caglayan, H.; Gordon, T. R.; Engheta, N.; Kagan, C. R.; Murray, C. B. Solution-Processed Phase-Change VO<sub>2</sub> Metamaterials from Colloidal Vanadium Oxide (VO<sub>x</sub>) Nanocrystals. *ACS Nano* **2014**, *8* (1), 797–806.